





Gemini, SOFIA, and ATCA Reveal Very Young, Massive Protostars in the Collapsing Molecular Cloud BYF 73

Rebecca L. Pitts¹ , Peter J. Barnes^{1,2}, Stuart D. Ryder^{3,4} , and Dan Li⁵¹ Astronomy Department, University of Florida, P.O. Box 112055, Gainesville, FL 32611, USA; rlpitts@ufl.edu² School of Science and Technology, University of New England, Armidale NSW 2351, Australia³ Department of Physics and Astronomy, Macquarie University, NSW 2109, Australia⁴ Australian Astronomical Observatory, 105 Delhi Road, North Ryde, NSW 2113, Australia⁵ National Optical Astronomy Observatory, 950 North Cherry Avenue, Tucson, AZ 85719, USA

Received 2018 June 30; revised 2018 October 3; accepted 2018 October 6; published 2018 October 25

Abstract

We present multi-wavelength data on the globally infalling molecular cloud/protostellar cluster BYF 73. These include new far-infrared (FIR) spectral line and continuum data from the Stratospheric Observatory for Infrared Astronomy's (SOFIA's) Far Infrared Field-Imaging Line Spectrometer (FIFI-LS), mid-infrared (MIR) observations with the Thermal-Region Camera Spectrograph (T-ReCS) on Gemini-South, and 3 mm continuum data from the Australia Telescope Compact Array (ATCA), plus archival data from *Spitzer*/Infrared Array Camera (IRAC), and *Herschel*/Photodetecting Array Camera and Spectrometer (PACS) and Spectral and Photometric Imaging Receiver (SPIRE). The FIFI-LS spectroscopy in [O I] λ 63 μ m, [O III] λ 88 μ m, [O I] λ 145 μ m, and [C II] λ 158 μ m highlights different gas environments in and between the dense molecular cloud and H II region. The photo dissociation region (PDR) between the cloud and H II region is best traced by [O I] λ 145 μ m and may have density $>10^{10} \text{ m}^{-3}$, but the observed λ 145 μ m/ λ 63 μ m and λ 63 μ m/ λ 158 μ m line ratios in the densest gas are well outside model values. The H II region is well-traced by [C II], with the λ 158 μ m/ λ 145 μ m line ratio, indicating a density of $10^{8.5} \text{ m}^{-3}$ and a relatively weak ionizing radiation field, $1.5 \lesssim \log(G/G_0) \lesssim 2$. The T-ReCS data reveal eight protostellar objects in the cloud, of which six appear deeply embedded ($A_V > 30^m$ or more) near the cloud's center. MIR 2 has the most massive core at $\sim 240 M_\odot$, more massive than all the others combined by up to tenfold, with no obvious gas outflow, negligible cooling line emission, and $\sim 3\%–8\%$ of its $4.7 \times 10^3 L_\odot$ luminosity originating from the release of gravitational potential energy. MIR 2's dynamical age may be as little as 7000 years. This fact, and the cloud's total embedded stellar mass being far less than its gas mass, confirm BYF 73's relatively early stage of evolution.

Key words: infrared: ISM – ISM: lines and bands – stars: formation – stars: protostars – submillimeter: ISM

1. Introduction

The formation of massive star clusters is a topic of active debate and study (Longmore et al. 2014, and references therein). Current questions include the timescale and mechanisms of gas mass assembly and star formation (Peretto & Fuller et al. 2013; Barnes et al. 2018), the degree to which gravity, turbulence, or magnetic fields control the dynamics (Crutcher 2012; Zamora-Avilés & Vázquez-Semadeni 2014; Padoan et al. 2016; Kobayashi et al. 2018), and the fidelity with which we can measure these effects with only trace constituents (Pitts et al. 2018).

BYF 73 (=G286.21+0.17, part of the Galactic Census of High and Medium-mass Protostars (CHaMP) survey of molecular clouds; Barnes et al. 2010, 2011) is one of only a dozen or so known parsec-scale molecular clumps that are undergoing large-scale collapse/contraction, but where only a few protostars have formed so far, and the cloud is still gas-dominated (Peretto & Fuller et al. 2013; Rygl et al. 2013; Wyrowski et al. 2016). With an estimated mass of $2 \times 10^4 M_\odot$ and luminosity of $10^4 L_\odot$, BYF 73 has the highest measured mass inflow rate, $0.034 M_\odot \text{ yr}^{-1}$, even among this extreme cohort (Barnes et al. 2010, 2016). Therefore, it may be in the early stages of forming a super star cluster like NGC 3603 in $\lesssim 0.5 \text{ Myr}$.

Such gas-dominated clouds are highly significant because the physical conditions, dynamics, and evolution must still be

close to the cloud's initial state, as opposed to even slightly more evolved objects like hot cores (Gerner et al. 2014), where the internal conditions are already dramatically altered by the energy input from luminous protostars. Therefore, a careful study of each such cloud will provide important boundary conditions for star formation theory. In this Letter, we present a range of new and archival data on BYF 73 from μ m to mm wavelengths, in order to examine the embedded protostellar content, gas mass distribution, and excitation conditions.

2. Observations and Data Reduction

2.1. *Spitzer*/Infrared Array Camera (IRAC)

BYF 73 was observed by the *Spitzer Space Telescope* in all four IRAC bands (3.6–8 μ m) as part of the Galactic Legacy Infrared Midplane Extraordinaire (GLIMPSE) survey (Benjamin et al. 2003). We downloaded calibrated public data from NASA's IRSA website, and transformed to Galactic coordinates for ease of comparison with data at other wavelengths. We cropped these data to cover all emission associated with the molecular cloud and its adjacent compact H II region, as in the $\sim 4'$ field shown in Figure 1. We measured the background-subtracted flux densities for the eight IRAC stellar sources that were also detected with the Thermal-Region Camera Spectrograph (T-ReCS; Section 2.2); these are plotted in Figure 3.

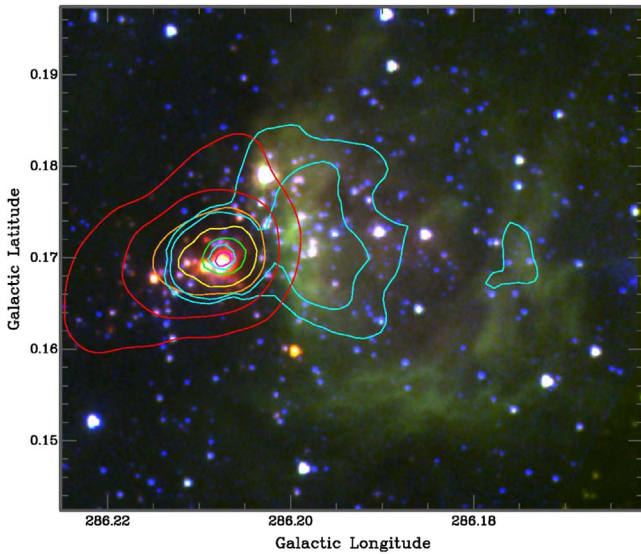


Figure 1. Composite image of *Spitzer* IRAC Bands 2 (red) and 1 (green), with *K* (blue) from the Anglo-Australian Telescope’s IRIS2 camera (Barnes et al. 2013). Contours are overlaid from *Herschel* and Australia Telescope Compact Array (ATCA) data: 500 μm (red, at 30% and 50% of the peak value), 350 μm (orange, 50%), 250 μm (yellow, 50%), 160 μm (green, 50%), 70 μm (cyan, 2%, 3%, 50%), and 3 mm (magenta, 67%). Note the clear separation between the molecular cloud to the left, and the compact H II region to the center and right.

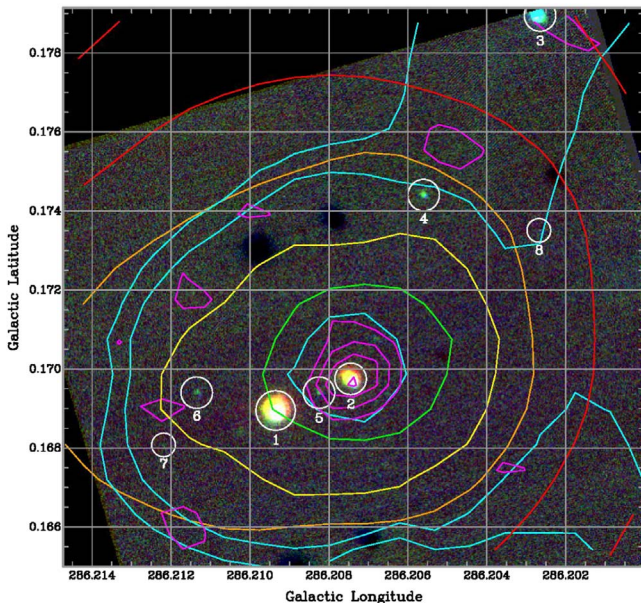


Figure 2. Identifications of point sources 1–8 detected in part of the $\sim 1'$ wide Gemini-South/T-ReCS mosaic. This composite image has colors (Qa = red, Si6 = green, Si2 = blue) indicating true flux ratio differences between these bands, and is overlaid by ATCA 3 mm continuum contours (magenta, from 14 mJy/bm spaced by 6 mJy/bm = 1σ) and the same far-infrared (FIR) contours as in Figure 1. The “dark” sources are negative images of the bright ones, due to the 15” chop-throw between the target and reference positions in the telescope observing mode. Sources MIR 1, 2, and 5–7 were imaged in all three positions, and so appear as bright objects, flanked 15” to the N and S by dark images. Sources MIR 4, 8, and 3 (barely) were imaged in the target and one reference position.

2.2. Gemini-South/T-ReCS

We obtained deep mid-infrared (MIR) data on BYF 73 with the high-resolution (point-spread function (PSF) $\approx 0''.3$) T-ReCS

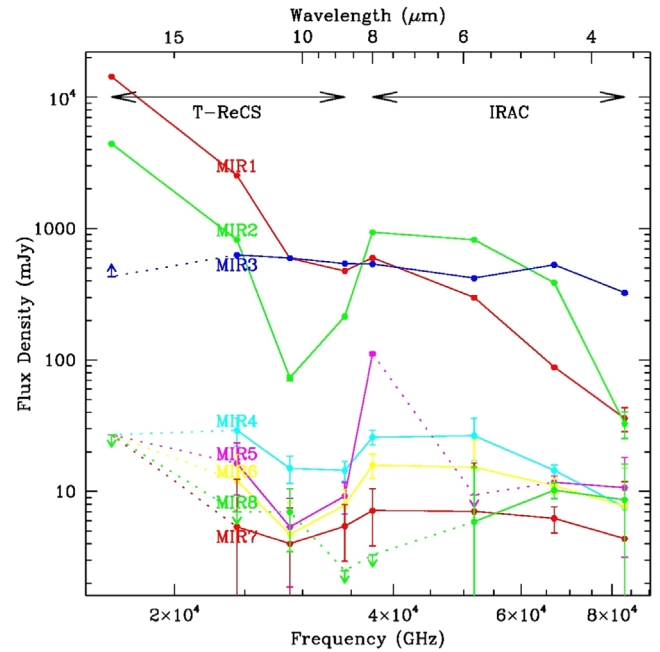


Figure 3. Flux densities of T-ReCS-detected sources in both T-ReCS and *Spitzer*/IRAC data. Secure detections are indicated by points connected by solid lines; 3σ upper limits are indicated by symbols connected to the other data by dotted lines. As we obtained only a partial image for MIR 3 at 18.3 μm , its flux density is at least twice the indicated lower limit. Error bars are 1σ noise values, but the calibration uncertainty is $\pm 15\%$ for these data after allowing for subtraction of variable background emission.

camera (Telesco et al. 1998) at Gemini-South on UT 2010 June 5–6, as part of program GS-2010A-Q-42 (PI: P. J. Barnes). The observations were set up to image a $1'$ field of view with a six-field mosaic of the $20'' \times 30''$ T-ReCS detector area, oriented to capture as many of the sources visible in the *Spitzer* images as possible. We cycled through the four filters Si2 (effective wavelength 8.74 μm), Si4 (10.4 μm), Si6 (12.3 μm), and Qa (18.3 μm) during the observing to form a commensurate set of images and enable multi-band photometry of all sources. Cohen et al. (1999) MIR standard stars SAO 250905 and SAO 222647 were observed before and after BYF 73, respectively, for flux calibration. The data were reduced with an in-house MIR data reduction package, which performed the chop-and-nod correction and co-added frames to form one image of BYF 73 at each MIR wavelength. Reduced and flux-calibrated images are presented in Figure 2 as a composite image of three of the four T-ReCS bands. The flux densities of the eight detected sources (based on aperture photometry with radii equal to three times the FWHM of the PSF) are included in the spectral energy distribution (SED) plot of Figure 3. For MIR 1, these are totals for both components of an equal-brightness binary, separated by $0''.38$ (PA = -14°) in the Si2 image, or 950 au assuming a distance of 2.5 kpc (Barnes et al. 2010). The other MIR sources show no evidence of binarity at this resolution.

2.3. Stratospheric Observatory for Infrared Astronomy/Far Infrared Field-Imaging Line Spectrometer (SOFIA/FIFI-LS)

We obtained integral-field spectra of BYF 73 centered on the [O I] $\lambda 63 \mu\text{m}$, [O III] $\lambda 88 \mu\text{m}$, [O I] $\lambda 145 \mu\text{m}$, and [C II] $\lambda 158 \mu\text{m}$ lines on 2016 July 1 and 3 UT with FIFI-LS (Colditz et al. 2012; Klein et al. 2014) on board SOFIA, as part of project 04-0061 (PI: P. J. Barnes). Chopping and nodding were done

asymmetrically due to the many nearby MIR sources to the (Galactic) west and south. Each integral field spectrum combines over 200 exposures dithered in sub-pixel increments to boost the sampling of the final spatially resampled image cube.⁶ The total integration times were 1659 s centered on the [C II] λ 158 μ m line, 3287 s on the [O I] λ 145 μ m line, 1628 s on the [O III] λ 88 μ m line, and 3318 s on the [O I] λ 63 μ m line. Pipeline processing with FLUXER⁷ includes fitting and separation of line and continuum emission components in each band, and telluric correction.

2.4. Herschel Photodetector Array Camera and Spectrometer (PACS) and Spectral and Photometric Imaging REceiver (SPIRE)

We obtained archival Level 3.5 data from the *Herschel* (Pilbratt et al. 2010) satellite’s PACS (Poglitsch et al. 2010) and SPIRE (Griffin et al. 2010) photometers, in order to combine with the other data described herein and fit SEDs across BYF 73 (see Section 3.2). The *Herschel* data were originally acquired as part of the Carina Nebula Complex (CNC) open time project (see Preibisch et al. 2012, for details).

2.5. Atacama Submillimeter Telescope Experiment (ASTE) and ATCA

The flux density at 850 μ m, 8 ± 1 Jy, is from a single-pointing measurement at the line emission peak, made with the 10 m ASTE (Ezawa et al. 2004) as part of another project (Y. Yonekura, private communication).

We observed BYF 73 at ATCA on 2010 October 1 and 4 UT in the H75 array (baselines \approx 31–89 m) in both the 94 ± 2 GHz continuum and the HCO⁺ and H¹³CO⁺ $J = 1 \rightarrow 0$ emission lines (89.19 GHz and 86.75 GHz, respectively) as part of program C2288 (PI: P. J. Barnes). We used the quasars 0537–441 and 1045–62, respectively, as passband and complex gain calibrators, and Mars as the flux calibrator. We mapped an 80-pointing mosaic of size 3.2 centered on the peak molecular line emission as measured in the Mopra maps (Barnes et al. 2010). Mediocre weather and poor phase stability, however, challenged the normal MIRIAD data reduction pipeline (Sault et al. 1995), resulting in line maps with low signal-to-noise ratios (S/N). The low spectral-line sensitivity was exacerbated by an apparently smooth intrinsic emission structure, as the ATCA HCO⁺ line flux was <30% of the Mopra single-dish value (Barnes et al. 2010), despite the short baselines. We fared better in the continuum, clearly detecting the point source MIR 2 at flux density 34 ± 7 mJy in the $5''.6 \times 4''.7$ synthesized beam (Figure 2). MIR 3 may also have been detected, but at $\sim 2\sigma$ this detection is not reliable; MIR 1 was not detected at all. Deconvolving MIR 2’s measured size, we obtain $4''.2 \times 3''.0 = 10,600 \times 7400$ au at 2.5 kpc for its physical dimensions at 3 mm, consistent with MIR 2 being a massive protostellar core.

⁶ See the FIFI-LS GI handbook at https://www.sofia.usra.edu/sites/default/files/FIFI-LS_GI_Handbook_RevB1.pdf, and the Cycle 5 SOFIA observer’s handbook at <https://www.sofia.usra.edu/science/proposing-and-observing/sofia-observers-handbook-cycle-5/5-instruments-ii-fifi-ls> for details of the spectral and spatial resolutions and observing modes.

⁷ <http://www.ciserlohe.de/fluxer/fluxer.html>

3. Analysis and Discussion

3.1. FIR Spectral Lines and Gas Conditions

To analyze the FIFI-LS data, we localized the overlap of contours of two or more line ratios/intensities on $\log(n_{\text{H}})$ – $\log(G/G_0)$ parameter maps from the Photo Dissociation Region Toolbox⁸ (PDRT; Kaufman et al. 2006; Pound & Wolfire 2008). Figure 4 shows the observed line intensity and derived $\log(n_{\text{H}})$ and $\log(G/G_0)$ maps, based on the PDRT and observed [C II] λ 158 μ m and [O I] λ 145 μ m line ratios. No line components were detected in [O III] λ 88 μ m. The [O I] λ 63 μ m fluxes were difficult to reconcile with the fluxes in the [O I] λ 145 μ m and [C II] λ 158 μ m lines, likely exacerbated by the [O I] λ 63 μ m line’s poor separation from the continuum in both the pipeline-processed spectra and our own alternative attempts. The [O I] λ 145 μ m/[C II] λ 158 μ m ratio and integrated [C II] λ 158 μ m line flux were enough to determine n and G/G_0 along the PDR to about half a dex precision, as shown in Figure 4. There, we derive $\log(G/G_0) \approx 1.5$ –2 and n_{H} ranging over $10^{10-11} \text{ m}^{-3}$.

Outside of the PDR, especially near MIR 1–2, PDRT’s built-in assumption of $A_V \leq 10^m$ breaks down, and there are no prescriptions for higher extinctions. G/G_0 did not noticeably change near MIR 1–3, but n fell where it was expected to rise. We found that the combination of weak [C II] λ 158 μ m line emission (at levels where PDRT flags as unreliable) and moderately high [O I] λ 145 μ m/[C II] λ 158 μ m ratios around MIR 1–3 create contours in the PDRT maps of n and G/G_0 that are nearly parallel over about three orders of magnitude in n (Figure 4).

While the [O I] λ 63 μ m/[O I] λ 145 μ m ratios do not provide further useful constraints on n or G/G_0 at most locations, near MIR 2 there is a suggestion of a distinct high-density peak in the gas ($10^{10.7} \text{ m}^{-3}$, not shown here), albeit with large uncertainty (~ 3 orders of magnitude in $\log n$). This is reflected in the slightly better-constrained three-line localization shown in Figure 4, where $\log n = 9.5^{+0.25}_{-1}$ at MIR 2. To check this, we determined the mass (and thus the density) and luminosity of MIR 2 from SED fitting (Section 3.3). Assuming MIR 2 is an ellipsoid with a line of sight depth similar to its observable dimensions (~ 9000 au), its volumetric mean density is $n = \rho / (\mu m_{\text{H}}) \approx 8 \times 10^{13} \text{ m}^{-3}$ (Section 3.3), close to PDRT’s mean+ 1σ value of n given the temperature and G/G_0 , and lending credence to the PDRT result despite its large uncertainty.

At these densities, in a relatively weak far-ultraviolet (FUV) field, and given that BYF 73 is on average cool and dense enough to have a CO-depleted center (Pitts et al. 2018), carbon should be locked up in CO. The measured line luminosities around MIR 2 are $\sim 7 \times 10^{-3} L_{\odot}$ in the [C II] λ 158 μ m line and $\sim 4 \times 10^{-3} L_{\odot}$ in the [O I] λ 145 μ m line. We conclude that in BYF 73, FIR “cooling” lines of O and C do not contribute significantly to the energy balance of the cloud, compared to the total FIR luminosity (Section 3.3).

3.2. MIR Point Sources

The MIR photometry reveals three features. First, we detect only six (proto)stars near the center of the molecular cloud, despite deep, high-resolution Very Large Telescope (VLT) *JHK* data showing ~ 30 heavily reddened objects ($J-K > 3$) in

⁸ <http://dustem.astro.umd.edu/pdrt/models1.html>

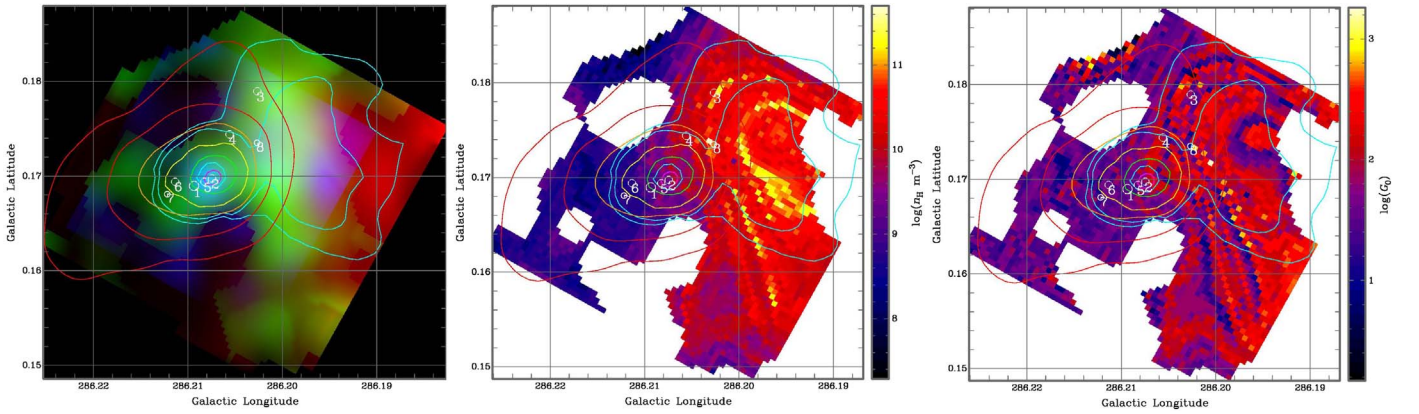


Figure 4. Left panel: composite image of [C II] $\lambda 158 \mu\text{m}$ intensity (red, normalized to $3.8 \times 10^{-7} \text{ W m}^{-2} \text{ sr}^{-1}$), [O I] $\lambda 145 \mu\text{m}$ (green, $6.4 \times 10^{-8} \text{ W m}^{-2} \text{ sr}^{-1}$), and [O I] $\lambda 63 \mu\text{m}$ (blue, $9.4 \times 10^{-11} \text{ W m}^{-2} \text{ sr}^{-1}$). Middle and right panels: respective images of derived $\log(n_{\text{H}})$ (m^{-3}) and $\log(G/G_0)$ (G_0 in Habing 1968 units, $1.6 \times 10^{-6} \text{ W m}^{-2}$), computed by localizing FIFI-LS line intensities/ratios on the PDRT parameters. Contours in all of the panels are the same as in Figure 1.

the same $30''$ -wide area (Andersen et al. 2017). The other two MIR stars, MIR 3 and 8, are either located within or projected onto the PDR front, and so may be slightly more evolved young stellar objects. The six central MIR stars may be the only true protostars in the imaged area, while the remaining near-infrared (NIR) objects may just be foreground pre-main sequence stars.

Second, only MIR 1–3 contribute significantly to the bolometric luminosity of the cloud. MIR 3–8 have slowly rising SEDs in the MIR, resembling classic Class II or III protostars (Adams et al. 1987; Barsony 1994; André & Montmerle 1994; MIR 5 seems to be brighter than expected in the IRAC Band 4 image, but is the most affected by blending with MIR 2, so this data point should be treated with caution.) Only the SEDs of MIR 1 and 2 show the steep rise at longer wavelengths expected of Class 0 or I protostars, although MIR 1 will need higher-resolution FIR data to separate it cleanly from its much brighter neighbor MIR 2. MIR 2 seems to fall between Class 0 and I definitions: it has a relatively high T_{bol} and low $L_{\text{submm}}/L_{\text{bol}}$, suggesting Class I, but very high gas fraction and infall rate, plus small age $t_{\text{inf}} = M/\dot{M} \sim 7000$ years, suggesting Class 0.

Third, all of the MIR stars except MIR 3 and 8 (the two stars possibly within the PDR) show absorption near $10 \mu\text{m}$, attributable to the $9.7 \mu\text{m}$ silicate feature and indicating the presence of intervening or circumstellar cold dust. For MIR 1 and 4–7, the absorption has a depth to 30%–50% of the adjacent $12 \mu\text{m}$ or $8 \mu\text{m}$ continuum, indicating dust with optical depths at $10 \mu\text{m}$ near 1. For MIR 2, however, the absorption is $>90\%$ of the MIR continuum, suggesting correspondingly larger amounts of dust, $\tau_{10} \sim 3 \pm 1$. Using a conversion of $A_V/\tau_{9.7} = 18.5 \pm 1.0$ magnitudes (Mathis 1990), we find approximate values of visual extinction toward each star of 54 ± 18^m (MIR 2) or 18 ± 5^m (others), though these conversions are for diffuse dust. In molecular clouds, this conversion shows substantial variation—often flattening at large A_V (Chiar et al. 2007)—so these extinction estimates are likely lower limits. Assuming further standard conversions of $N_{\text{H}} = 1.87 \times 10^{25} \text{ m}^{-2} A_V \approx 2N_{\text{H}_2}$ in these clouds (Gerin & Liszt 2017), where the HI contribution to the total column density is assumed to be small, $\Sigma = 1.88 M_{\odot} \text{ pc}^{-2} (N_{\text{H}_2}/10^{24} \text{ m}^{-2})$ (Barnes et al. 2018), and multiplying by 2 to account for the rear half of each core, we obtain corresponding (very approximate) total mass columns from

the silicate absorption of $1950 \pm 650 M_{\odot} \text{ pc}^{-2}$ (MIR 2) and $650 \pm 190 M_{\odot} \text{ pc}^{-2}$ (others). If we assume a fiducial envelope size of 10^4 au (Adams et al. 1987), the total masses (better estimated in Section 3.3) are $\sim 110 \pm 40 M_{\odot}$ for MIR 2 and $\sim 40 \pm 10 M_{\odot}$ for the others. As we show below, this approach is a case in point for the caution urged by Gerin & Liszt (2017).

3.3. FIR/Sub-mm Continuum SED Fitting

To compute the core masses for the MIR point sources, we cropped and regridded the *Herschel* and SOFIA [O I] $\lambda 63 \mu\text{m}$ continuum images to the area and pixel grid of the FIFI-LS [C II] image, and experimented with fitting up to three 2D Gaussian PSFs at each wavelength, fixed at their respective MIR positions. MIR 1 and 2 are $7''.4$ apart, fortuitously aligned with the minor axes of the PACS beams, so they are separable at 63 and $70 \mu\text{m}$, but not at longer wavelengths. MIR 5 is too close to both MIR 1 and 2 to be separable by *Herschel* or SOFIA, but shorter-wavelength data (Figure 3) already suggest that MIR 3–8 contribute negligibly in the FIR, compared to MIR 1–2; even MIR 3 is undetected as a resolved object for $\lambda > 30 \mu\text{m}$.⁹ At 63 and $70 \mu\text{m}$, we fit Gaussians and background levels to minimize the residuals at MIR 1 and 2. At longer wavelengths, we estimated the contribution of MIR 1 by comparing the shape of the PSF at MIR 2 on the side facing MIR 1, to that on the opposite side. We then integrated the Gaussian models for each core separately at each wavelength, without the background.

We fit the resulting fluxes with a modified Planck function of the form $I_{\nu} = F_{\nu}/\Omega \approx B_{\nu}(T_{\text{d}})[1 - e^{-\tau}]$ with $\tau = (\nu/\nu_0)^{\beta} N_{\text{H}_2} \mu m_{\text{H}} \kappa_0/\gamma$. Here, $B_{\nu}(T_{\text{d}})$ is the Planck function at dust temperature T_{d} ; Ω is the solid angle of the source; β is the dust emissivity index; κ_0 is the dust opacity coefficient at fiducial frequency ν_0 (we use 1200 GHz); N_{H_2} is the fitted H_2 column density; γ is the gas-to-dust mass ratio; $\mu = 2.8$ is the mean molecular weight per hydrogen molecule; and m_{H} is the mass of the hydrogen atom. T_{d} and N_{H_2} were allowed to vary, while γ was fixed at 100 (Beckwith et al. 1990), β at 2.0 (Bianchi et al. 1999, and references therein), and $\kappa_0 = \kappa(350 \mu\text{m}) \approx 0.2 \text{ m}^2 \text{ kg}^{-1}$ (e.g., Liseau et al. 2015). For MIR 2, we used Ω from the ATCA interferometry, 14.3 arcsec^2 (see Section 2.5 for dimensions), as a representative core size ($D^2\Omega = 2.09 \times 10^{-3} \text{ pc}^2$ where $D = 2.5 \text{ kpc}$). MIR 1 is only

⁹ There is extended FIR/sub-mm structure in the direction of MIR 6–7, but we doubt either of these sources contributes meaningfully to this emission.

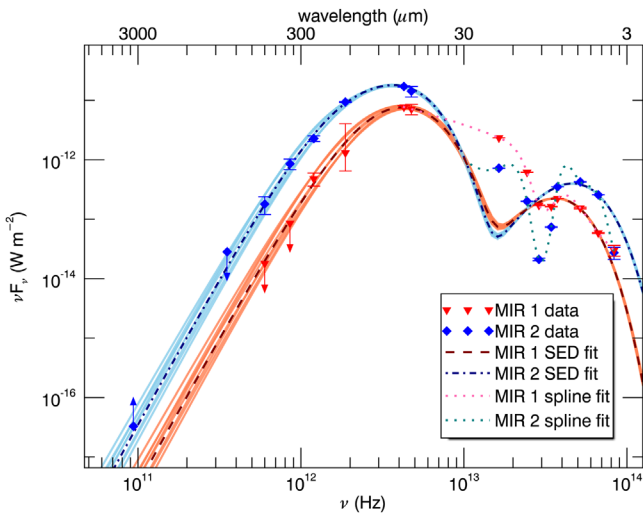


Figure 5. Two-component SED fits to MIR 1 and 2. The model used does not fit the $10\ \mu\text{m}$ silicate feature or small grain emission.

resolved in the IRAC $3.6\ \mu\text{m}$ band, so we estimated MIR 1’s deconvolved core dimensions to be $1''.9 \times 1''.6$ ($D^2\Omega = 5.1 \times 10^{-4}\ \text{pc}^2$), noting that the IRAC $3.6\ \mu\text{m}$ filter passband encloses the $3.29\ \mu\text{m}$ polycyclic aromatic hydrocarbon (PAH) line, which is correlated with dust emission (Jones et al. 2015).

Two-component SED fitting of ATCA, ASTE, *Herschel*, SOFIA-63 μm , and *Spitzer*/IRAC data yields $N_{\text{H}_2} = 6.2_{-1.7}^{+3.6} \times 10^{28}\ \text{m}^{-2}$ in $T_d = 44.8 \pm 0.4\ \text{K}$ gas for MIR 2, and $N_{\text{H}_2} = 2.1_{-0.5}^{+1.3} \times 10^{28}\ \text{m}^{-2}$ in $T_d = 51 \pm 1\ \text{K}$ gas for MIR 1 (see Figure 5). We only included additional warm temperature components to verify that they contributed negligibly to the total mass column and to estimate the total luminosity; their parameters are unreliable. The formal errors are based on the standard errors of the model fluxes used in fitting and the reported calibration errors of T-ReCS and the *Herschel* instruments. The total uncertainty of N_{H_2} may be a factor of two or more due to the uncertainty in γ (Reach et al. 2015). The $9.7\ \mu\text{m}$ silicate absorption feature is not part of the model, and neither is stochastic heating.

For MIR 2, the above column density corresponds to $\tau_{\text{MIR}2}(70\ \mu\text{m}) \approx 14$, $A_V \sim 7000^m$, and $\Sigma_{\text{MIR}2} = 1.2_{-0.4}^{+0.3} \times 10^5\ M_\odot\ \text{pc}^{-2}$, where the warm component’s contribution is negligible. These values look extreme, but over the representative size of MIR 2 at 3 mm, the core mass works out to a reasonable $240_{-50}^{+80}\ M_\odot$. The total luminosity of MIR 2 is $4700_{-500}^{+100}\ L_\odot$, of which about $4500L_\odot$ is from the $T_d = 45\ \text{K}$ component alone. Despite being only a few percent of BYF 73’s total mass and not much warmer than the clump on average (Pitts et al. 2018), MIR 2 contributes nearly half the total luminosity. Deepening the mystery, if $\dot{M} = 0.034 \pm 0.017\ M_\odot\ \text{yr}^{-1}$ (Barnes et al. 2010) and $R \approx 4500\ \text{au}$, the gravitational contraction luminosity is $L_g = GMMR^{-1} \approx 260\ L_\odot$, much more than the line luminosity but still only $\sim 6\%$ of MIR 2’s total.

For MIR 1, by the same analysis, $\tau_{\text{MIR}1}(70\ \mu\text{m}) \sim 5$ and $\Sigma_{\text{MIR}1} \approx 4_{-2}^{+3} \times 10^4\ M_\odot\ \text{pc}^{-2}$, corresponding to a core mass of about $20_{-10}^{+20}\ M_\odot$. The cool dust component of MIR 1 contributes $1100 \pm 100\ L_\odot$ to the total luminosity. The T-ReCS 12 and $18\ \mu\text{m}$ data could only be included in the fit with a spline (which was only used to estimate the total

luminosity), but this raised MIR 1’s total luminosity to $\sim 1900L_\odot$. These T-ReCS data points cannot trace the same temperature component as the FIR data, because that would indicate a $1\ M_\odot$ protostar with a $4000L_\odot$ luminosity.

For MIR 3, given the background flux levels in the *Herschel* data and its non-detection at $\lambda \geq 30\ \mu\text{m}$, MIR 3 can be no more than $\sim 10\%$ of the mass of MIR 1. If the same holds for MIR 4–8 as indicated by the FIR non-detections, MIR 2 has nearly 10 times the mass of the other seven objects put together.

4. Concluding Remarks

The mass and volume density of MIR 2 is comparable to the larger of two massive cores in SDC 335 (Peretto & Fuller et al. 2013), a similar molecular clump to BYF 73 undergoing a massive inflow of gas toward its central objects, but in the case of SDC 335 through a prominent network of accreting filaments. BYF 73 is different because the inflow observed in the single-dish data (resolution $40''$) is across a cloud structure smooth enough to start resolving out on scales $\lesssim 30'' \approx \frac{1}{3}\ \text{pc}$. Furthermore, while the two cores in SDC 335 account for about 10% of the total mass of that cloud, MIR 2 is potentially $\sim 10\times$ as massive as MIR 1 and MIR 3–8 combined, yet accounts for only about 1% of BYF 73’s total mass: it is $\gtrsim 98\%$ gas. This result means BYF 73 may represent an even earlier stage of massive star formation than SDC 335, such that much of the cloud still shows signs of CO freeze-out and has detectable sublimation fronts facing both NGC 3324 and the adjacent compact H II region (Pitts et al. 2018). In the hunt for the elusive transition from starless core to massive Class 0 protostar, the cores in BYF 73 may be the closest yet seen.

We thank the SOFIA crew and Gemini-South and *Spitzer* staff for outstanding support of their respective telescopes, Vicki Lowe for help with the ATCA observing, and the anonymous referee for several helpful suggestions which improved the paper. R.L.P. and P.J.B. gratefully acknowledge support from grants NASA-ADAP NNX15AF64G and SOF 04-0061. The Australia Telescope Compact Array is part of the Australia Telescope National Facility which is funded by the Australian Government for operation as a National Facility managed by CSIRO. Based on observations obtained at the Gemini Observatory, which is operated by the Association of Universities for Research in Astronomy, Inc., under a cooperative agreement with the NSF on behalf of the Gemini partnership: the National Science Foundation (United States), the National Research Council (Canada), CONICYT (Chile), Ministerio de Ciencia, Tecnología e Innovación Productiva (Argentina), and Ministério da Ciência, Tecnologia e Inovação (Brazil).

Facilities: ATCA, SOFIA(FIFI-LS), Gemini:South(T-ReCS), *Spitzer*(IRAC), *Herschel*(PACS, SPIRE).

ORCID iDs

Rebecca L. Pitts  <https://orcid.org/0000-0002-7937-4931>
Stuart D. Ryder  <https://orcid.org/0000-0003-4501-8100>

References

- Adams, F. C., Lada, C. J., & Shu, F. H. 1987, *ApJ*, 312, 788
Andersen, M., Barnes, P. J., Tan, J. C., Kainulainen, J., & de Marchi, G. 2017, *ApJ*, 850, 12

- André, P., & Montmerle, T. 1994, *ApJ*, **420**, 837
- Barnes, P. J., Hernandez, A. K., Muller, E., & Pitts, R. L. 2018, *ApJ*, **866**, 19
- Barnes, P. J., Hernandez, A. K., O'Dougherty, S. D., Schap, W. J., III, & Muller, E. 2016, *ApJ*, **831**, 67
- Barnes, P. J., Ryder, S. D., O'Dougherty, S. N., et al. 2013, *MNRAS*, **432**, 2231
- Barnes, P. J., Yonekura, Y., Fukui, Y., et al. 2011, *ApJS*, **196**, 12
- Barnes, P. J., Yonekura, Y., Ryder, S. D., et al. 2010, *MNRAS*, **402**, 73
- Barsony, M. 1994, *ASPCS*, **65**, 197
- Beckwith, S. V. W., Sargent, A. I., Chini, R. S., & Guesten, R. 1990, *AJ*, **99**, 924
- Benjamin, R. A., Churchwell, E., Babler, B. L., et al. 2003, *PASP*, **115**, 953
- Bianchi, S. 2013, *A&A*, **552**, A89
- Bianchi, S., Davies, J. I., & Alton, P. B. 1999, *A&A*, **344**, L1
- Chiar, J. E., Ennico, K., Pendleton, Y. J., et al. 2007, *ApJL*, **666**, L73
- Cohen, M., Walker, R. G., Carter, B., et al. 1999, *AJ*, **117**, 1864
- Colditz, S., Fumi, F., Geis, N., et al. 2012, *Proc. SPIE*, **8446**, 844617
- Crutcher, R. M. 2012, *ARA&A*, **50**, 29
- Ezawa, H., Kawabe, R., Kohno, K., & Yamamoto, S. 2004, *Proc. SPIE*, **5489**, 763
- Gerin, M., & Liszt, H. 2017, *A&A*, **600**, A48
- Gerner, T., Beuther, H., Semenov, D., et al. 2014, *A&A*, **563**, 97
- Griffin, M. J., Abergel, A., Abreu, A., et al. 2010, *A&A*, **518**, L3
- Habing, H. J. 1968, *BAN*, **19**, 421
- Jones, A. G., Bendo, G. J., & Baes, M. 2015, *MNRAS*, **448**, 168
- Kaufman, M. J., Wolfire, M. G., & Hollenbach, D. J. 2006, *ApJ*, **644**, 283
- Klein, R., Beckmann, S., Bryant, A., et al. 2014, *Proc. SPIE*, **9147**, 91472X
- Kobayashi, M. I. N., Kobayashi, H., Inutsuka, S., & Fukui, Y. 2018, *PASJ*, **70**, S59
- Liseau, R., Larsson, B., Lunttila, T., et al. 2015, *A&A*, **578**, A131
- Longmore, S. N., Kruijssen, J. M. D., Bastian, N., et al. 2014, in *Protostars and Planets VI*, ed. H. Beuther et al. (Tucson, AZ: Univ. Arizona), 291
- Mathis, J. S. 1990, *ARA&A*, **28**, 37
- Padoan, P., Pan, L., Haugbølle, T., & Nordlund, Å. 2016, *ApJ*, **822**, 11
- Peretto, N., Fuller, G. A., Duarte-Cabral, A., et al. 2013, *A&A*, **555**, 112
- Pilbratt, G. L., Riedinger, J. R., Passvogel, T., et al. 2010, *A&A*, **518**, L1
- Pitts, R. L., Barnes, P. J., & Varosi, F. 2018, *MNRAS*, submitted
- Poglitsch, A., Waelkens, C., Geis, N., et al. 2010, *A&A*, **518**, L2
- Pound, M. W., & Wolfire, M. G. 2008, in *ASP Conf. Ser. 394*, *Astronomical Data Analysis Software and Systems XVII*, ed. R. W. Argyle et al. (San Francisco, CA: ASP), 654
- Preibisch, T., Roccatagliata, V., Gaczkowski, B., & Ratzka, T. 2012, *A&A*, **541**, A132
- Reach, W. T., Heiles, C., & Bernard, J. P. 2015, *ApJ*, **811**, 118
- Rygl, K. L. J., Wyrowski, F., Schuller, F., & Menten, K. M. 2013, *A&A*, **549**, 5
- Sault, R. J., Teuben, P. J., & Wright, M. C. H. 1995, in *ASP Conf. Ser. 77*, *Astronomical Data Analysis Software and Systems IV*, ed. R. A. Shaw et al. (San Francisco, CA: ASP), 433
- Telesco, C. M., Pina, R. K., Hanna, K. T., et al. 1998, *Proc. SPIE*, **3354**, 534
- Wyrowski, F., Güsten, R., Menten, K. M., et al. 2016, *A&A*, **585**, A149
- Zamora-Avilés, M., & Vázquez-Semadeni, E. 2014, *ApJ*, **793**, 84